Journal of Colloid and Interface Science 579 (2020) 862–871

Contents lists available at ScienceDirect

Journal of Colloid and Interface Science

journal homepage: www.elsevier.com/locate/jcis

Self-assembly of carbon nanotube/graphitic-like flake/BiOBr nanocomposite with 1D/2D/3D heterojunctions for enhanced photocatalytic activity

Weiwei Tie [a,b], Zhaoyu Du [a,b], Hongwei Yue [a,b], Surjya Sarathi Bhattacharyya [d], Zhi Zheng [a,b], Weiwei He [a,b,*], Seung Hee Lee [b,c,*]

[a] Key Laboratory of Micro-Nano Materials for Energy Storage and Conversion of Henan Province, College of Chemical and Materials Engineering, Institute of Surface Micro and Nano Materials, Xuchang University, Henan 461000, China
[b] Henan Joint International Research Laboratory of Nanomaterials for Energy and Catalysis, Xuchang University, Xuchang, Henan 461000, China
[c] Applied Materials Institute for BIN Convergence, Department of BIN Convergence Technology and Department of Polymer Nano-Science and Technology, Jeonbuk National University, Jeonju, Jeonbuk 54896, South Korea
[d] Asutosh College, 92, Shyamaprasad Mukherjee Road. Kolkata 700 026, West Bengal, India

GRAPHICAL ABSTRACT

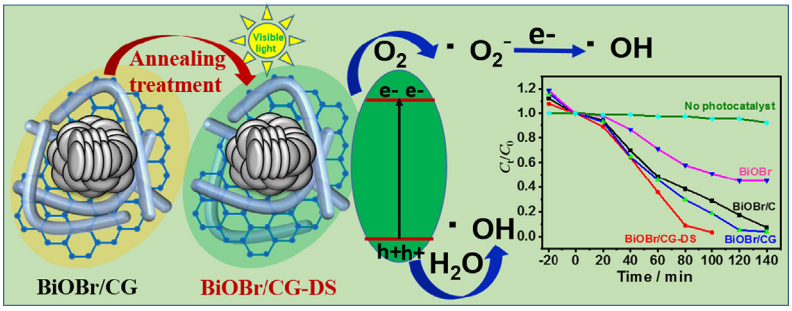

ARTICLE INFO

Article history:
Received 21 May 2020
Revised 17 June 2020
Accepted 21 June 2020
Available online 27 June 2020

Keywords:
BiOBr
Carbon nanotubes
Reduced graphitic oxide
Photocatalytic degradation
Self-assembly

ABSTRACT

A self-assembled nanocomposite of lamellar BiOBr covalently bonded with conductive network of dispersive one-dimensional carbon nanotubes (1D CNT) and two-dimensional reduced graphitic-like flakes (2D GF) had been in situ constructed using one-pot facile solvothermal technique. Through self-assembly, BiOBr/CNT/GF (BiOBr/CG) displayed three-dimensional architectures in which a strong interfacial contact interaction and covalent banding between BiOBr nanostructures and CNT/GF network appeared. Furthermore, visible-light-driven catalytic activity of BiOBr/CG for RhB dye degradation was superior to that of pure BiOBr or BiOBr/C. Interestingly, the photodegradation activity of the BiOBr/CG nanocomposite could be improved further by subsequent facile annealing treatment, in which the annealed BiOBr/CG-DS had degraded almost 97.9% of RhB dye within only 100 min of visible-light irradiation. Moreover, analysis of the photodegradation mechanism revealed that the repression of electron-hole recombination in the nanocomposites, with sufficient covalent interfacial contact with CNT/GF as effective electron collecting and transferring system, were responsible for the outstanding photocatalytic performance. This effect, in turn, led to the continuous generation of $\cdot O^{2-}$ and ·OH reactive oxygen species for the degradation of RhB dye, which was verified by active species trapping and ESR spectra.

* Corresponding authors at: Henan Joint International Research Laboratory of Nanomaterials for Energy and Catalysis, Xuchang University, Xuchang, Henan 461000, China.
E-mail addresses: heweiweixcu@gmail.com (W. He), lsh1@jbnu.ac.kr (S. Hee Lee).

https://doi.org/10.1016/j.jcis.2020.06.088
0021-9797/

1. Introduction

In the management and treatment of serious environmental pollution, an efficient and environmental friendly purification method is greatly desired. One technology that has been considered for this application is semiconductor photocatalysis, and recently, various types of semiconductor photocatalysts have been developed and explored, which can utilize sunlight energy to degrade pollutants directly and effectively [1–4]. Among the numerous photocatalysts, lamellar BiOBr has high visible photocatalytic oxidation and reduction activity because of its appropriate band-gap (2.75 eV) providing enough space to polarize the $[Bi_2O_2]$ layers and interleaved double sheets of Br atoms, which then in turn induces strong internal static electric fields between the $[Bi_2O_2]$ layer and Br slabs [5,6]. These actions promote the separation of photogenerated electron-hole pairs enabling the wide application of lamellar BiOBr in the photocatalytic degradation (PCD) of organic dyes and other pollutants. To further improve their photocatalytic performance, many efforts have been focused onto construction of 3D hierarchical structures [7], or elemental doping [6], or crystal facet engineering with specific exposed facets and crystal sizes [8,9]. It has been reported that [001] facet normally displays reactively higher photocatalytic activity than the (010) facets [9]. Additionally, the fabrication of carbon-based composites or heterojunctions by effective microstructure control or efficient electron transport has also drawn much attention [10,11].

For this task, carbon materials, including carbon nanotubes, carbon quantum dots, graphene, and graphene quantum dots, are appropriate candidates due to their superior optical and excellent electron-transfer properties [12–15]. Among these materials, graphene flakes, carbon nanotubes, as single or multilayered graphene sheets and their nanometer-size cylindrical tubes, are ideal one- or two-dimensional structures. Indeed, the basic constituent of carbon nanotubes (CNTs) is graphite, and they exhibit excellent optical absorption and electron-transfer properties [16,17]. Although a variety of carbon based BiOBr nanocomposites with improved photocatalytic activity have been developed, to our knowledge, there has been very little systematic research reported on a multidimensional graphitic-like structure to aid in the performance of BiOBr photocatalysts by providing abundant photocatalytic active sites and shortening the electron-transfer distance [11–14]. It has been reported that carbon nanotube/reduced graphene oxide (CNT/RGO) hybrids with dispersible graphene and CNTs have much higher electrical conductivities than those of pure graphene or pure CNT film [17]. Maarouf A.A., et al. has also reported that a graphene-con ducting-carbon-nanotube hybrid system has high application potential as a transparent electrode in photovoltaic applications because it has higher conductivity than pristine graphene [18]. Therefore, because of the efficient interfacial interaction when the same substrate is co-modified with different dimensions of graphitic-like structures, it is expected that enhanced photovoltaic properties could be obtained over those of bare graphene or CNT itself. It is also reasonable to assume one ideal and possible route to optimize the performance of the BiOBr semiconductor ingredients would be to combine individual 1D CNTs and 2D RGO together with the BiOBr semiconductor ingredients fully and intimately in order to synergistically improve the original electrical conductivity of CNT/RGO hybrids. In this scenario, because the CNTs could act as conducting bridges with an increased number of contact sites between RGO and CNTs, they would then form effective conductive paths between the RGO sheets, by which we could maximize their excellent electron conductivity through the sufficient interfacial contact between carbon materials and the semiconductor. As a result, upon light irradiation, the semiconductors yield photogenerated electron-hole pairs with a lifetime that could be prolonged much more effectively than if they are generated with simple integration of pure RGO and semiconductors, for which the interfacial contact between the BiOBr and RGO is rather insufficient due to the strong tendency of the reported flat BiOBr sheets to restack with one another and less numerous contacts between only the RGO sheets [19]. Therefore, for the synthesis of high efficiency photocatalytic products for practical applications, the benefit of an efficacious electron transfer system that presents sufficient interfacial contacts between BiOBr and CNT/graphene conductive pathways, resulting in abundant catalytic active sites and short charge-transfer distance should not be overlooked.

Herein, we have reported a solution-based method to fabricate the self-assembled BiOBr/CG heterostructure through a one-step in situ solvothermal reaction that does not require any expensive chemicals. This method sufficiently utilizes dispersible conjugated carbon with oxygen-containing groups in an aqueous or organic phase, thereby resulting in excellent interfacial contact between BiOBr and the graphitic-like surface. The synthesized samples are confirmed by multiple characterization techniques, and their photocatalytic activities are evaluated through the degradation of Rhodamine B (RhB) under visible light irradiation. The resulting data reveals that the introduction of a dispersive 2D GF and 1D CNTs into this self-assembled BiOBr/CG heterostructure not only could efficiently prevent them from restacking with each other, thus endowing them excellent physiochemical stability, but it also achieves the ultimate purposes of broadly absorbing solar light, reducing the recombination of photogenerated electron-hole pairs, as well as the high-speed transfer of the excited electrons from the semiconductor surface. Furthermore, we have investigated and discussed the promoting effect of the calcination procedure on its photocatalytic performance and its mechanism in detail.

2. Experimental

2.1. Materials

$Bi(NO_3)\cdot 5H_2O$ (>99%), ethylene glycol, Rhodamine B (RhB), and ethanol were obtained from China Reagent Company, LTD. All chemicals were of analytical grade, and were used as received without further purification. To prepare the BiOBr/CG photocatalytic composites, the used multi-walled carbon nanotube (CNT) purchased by the Chinese Academy of Sciences in Sichuan (China) was further acid oxidized via an improved acid oxidation procedure, hereafter named f-CNT [20]. The highly purified (>99%) natural graphite flakes (320 mesh), supplied by Alfa Aesar, were modified with the improved Hummers' method utilizing chemical oxidization and sonication exfoliation, to obtain what it was hereafter called graphitic oxide (GO) [21].

2.2. Synthesis of BiOBr/CG

In a typical procedure, the hybrid catalysts were prepared through a modified BiOBr synthesis program [6]: different amounts of 6 mg/ml graphitic oxide (0.2 ml mg, 0.5 mg, and 1 mg) and oxidized CNT (2 mg) were ultrasonically dispersed into ethylene glycol (10 ml) for 1 h in order to obtain homogeneous dispersion. Soon afterwards, $Bi(NO)_3\cdot 5H_2O$ (0.73 g) and KBr (0.82 g) were dissolved into fresh ethylene glycol (10 ml) with continuous stirring, and then the above-mentioned homogeneous solutions were mixed and then transferred to a Teflon-sealed autoclave for reaction at 170 °C for 6 h. Finally, the products were washed

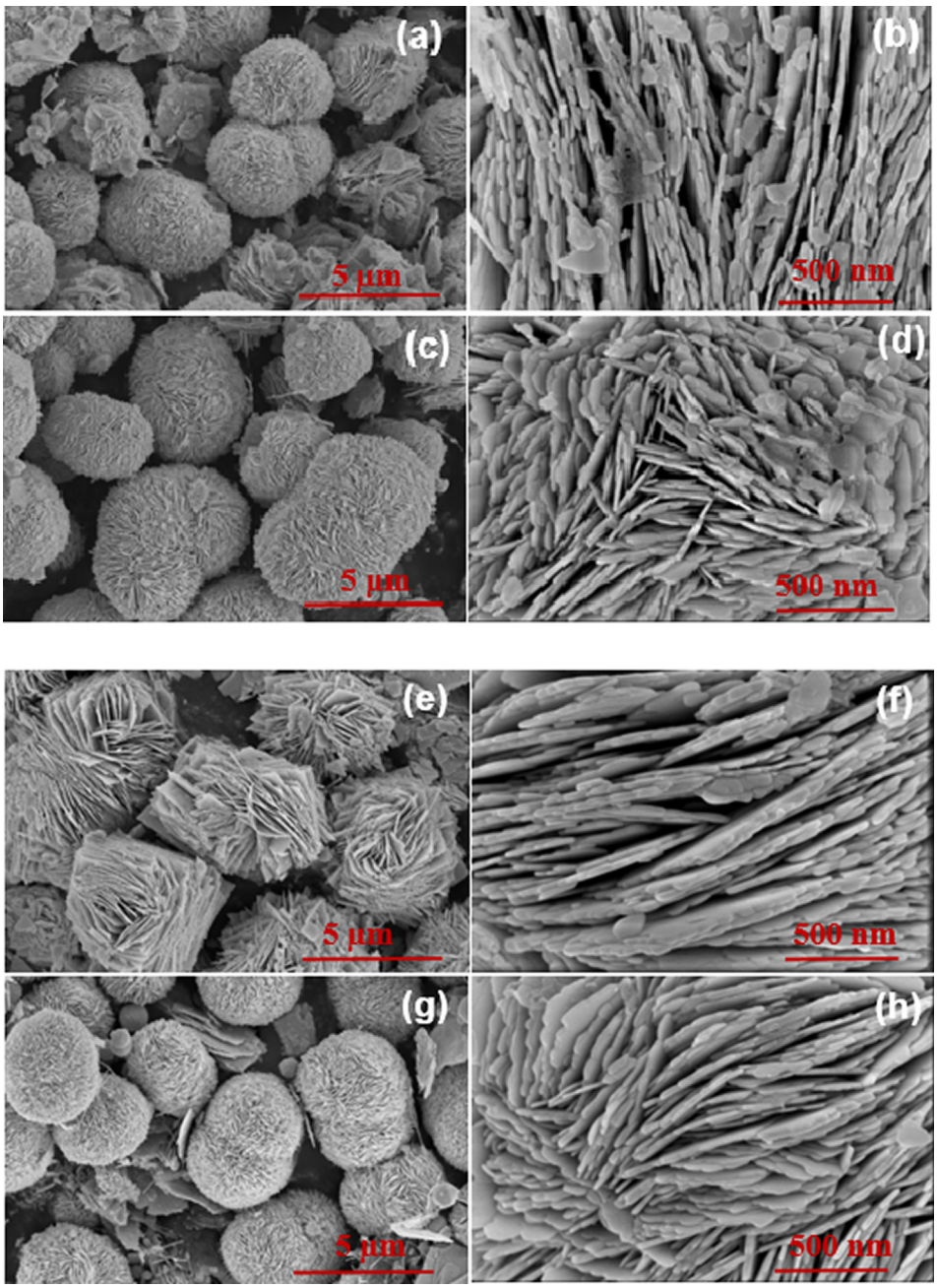

Fig. 1. SEM micrographs of the BiOBr/CG (a, b), BiOBr/CG-DS (c, d) hybrid, BiOBr (e, f) BiOBr/C(g, h).

several times with distilled water and ethanol, and then dried in vacuum at 40 °C for 12 h, hereafter calling after BiOBr/CG, BiOBr/CG-2 and BiOBr/CG-3) For comparison, pure BiOBr or BiOBr/C was also obtained utilizing a similar procedure without oxidized CNT or graphitic oxide, which were called after BiOBr or BiOBr/C, respectively. Additionally, BiOBr/CG was further modified by subjecting it to supplementary annealing at 400 °C in air for 2 h, hereafter calling after BiOBr/CG-DS.

2.3. Characterization

X-ray diffraction (XRD) pattern was recorded with an X-ray diffractometer (Bruker D8 Advance) using Cu-Kα radiation (λ = 1. 5406 Å) for crystal structure analysis, and the average crystallite size of the synthesized samples was calculated using the Scherrer's formula ($D = K\lambda/\beta \cos\theta$) [22,23]. The morphologies and microstructures of the synthesized samples could be examined using an electron microscope (SEM, FEI Nova NanoSEM 450) and transmission electron microscope (TEM, Jeol Jem-2100F). Fourier transform infrared (FT-IR) spectra were measured with the Thermo Nicolet6700 using the KBr pellet technique. The confocal Raman spectrum was obtained using the confocal Raman system with 532 nm He: Ne laser (Renishaw in Via). The surface elements and chemical states of the synthesized samples were determined using X-ray photoelectron spectroscopy (XPS) with an XPS spectrometer (Thermo Escalab 250XI, USA) and Al-Kα radiation (hν = 1486.6 eV). UV–vis diffuse reflectance spectroscopy (DRS) was performed using a Cary 5000 UV–vis-NIR spectrophotometer. Next, the Photoluminescence (PL) spectroscopic characterization was obtained with a Hitachi F-4600 fluorescence spectrophotometer. The surface

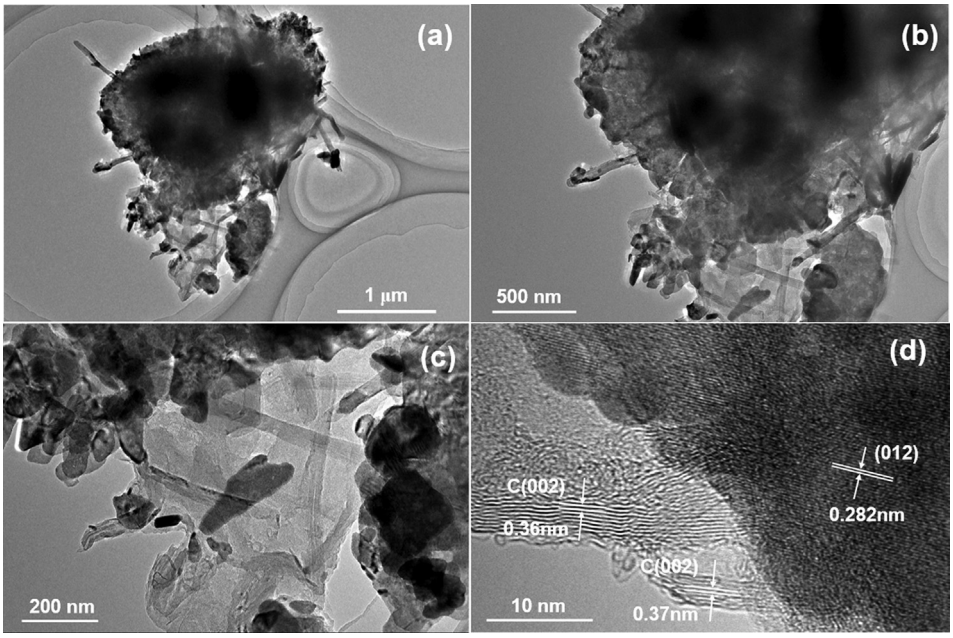

Fig. 2. TEM micrographs of the BiOBr/CG-DS hybrid at different magnifications (a, b, c). High-resolution TEM micrographs of the BiOBr/CG-DS hybrid (d).

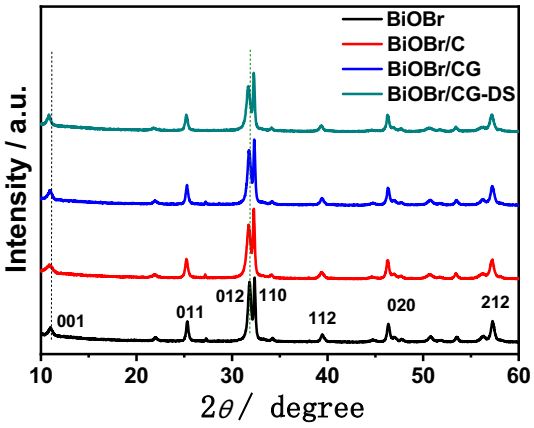

Fig. 3. XRD patterns of pure BiOBr and its compound.

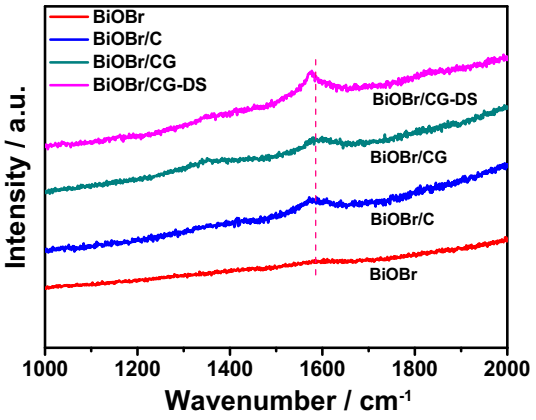

Fig. 4. Raman spectra of pure BiOBr, BiOBr/C, and BiOBr/CG.

photovoltage (SPV) measurements were made through sandwiched capacitor consisting two FTO substrates with interposition of powdered samples and a piece of mica placed between the film-like sample and bottom FTO substrate made using the laser pulse (355 nm with a pulse width of 4 ns) as reported by Y. Lei et al [24]. Photocurrent measurements as a function of time with switching on and off cycles were carried out using a conventional three-electrode system with the electrochemical workstation (CH Instruments, CHI 660) in 0.1 M KCl electrolyte under simulated sunlight irradiation (approximately 100 mW/cm^2) [11,25].

2.4. Photocatalytic activity

The photocatalytic activity of the synthesized BiOBr samples was evaluated through the degradation of an aqueous Rhodamine B solution under visible light irradiation. The visible light was provided by a 500 W Xe lamp with an UV cutoff filter ($\lambda \geq 420$ nm), and a series of synthesized BiOBr-based samples (10 mg) were added to 50 ml of the Rhodamine B solution (10 mg/L) with sufficient stirring in dark to ensure adsorption/desorption equilibrium. After that, the suspension was removed from the reactor at regular time intervals under visible light irradiation. After centrifugation, the concentration of Rhodamine B as a function of irradiation time around 554 nm was analyzed by UV/vis spectroscopy (Agilent Cary-5000). The photocatalytic activity was calculated according to $\varphi = C_t/C_0$, where φ is considered the degradation efficiency, and C_t and C_0 represent the concentration of RhB in the solution at the time taken out in the photocatalytic process of t and 0, respectively [26]. The active species during the photodegradation reaction were determined by dissolving different scavengers, such as methanol, potassium permanganate ($KMnO_4$), *t*-butyl alcohol (TBA), and benzoquinone (BQ), which could capture photo-induced holes and electrons as well as their corresponding **.**OH radicals and $\cdot O_2^-$ radicals, respectively [11,26,27].

3. Results and discussion

3.1. Morphology and microstructure analysis

We have investigated the morphology and microstructures of the samples by SEM and TEM, the results from which are shown

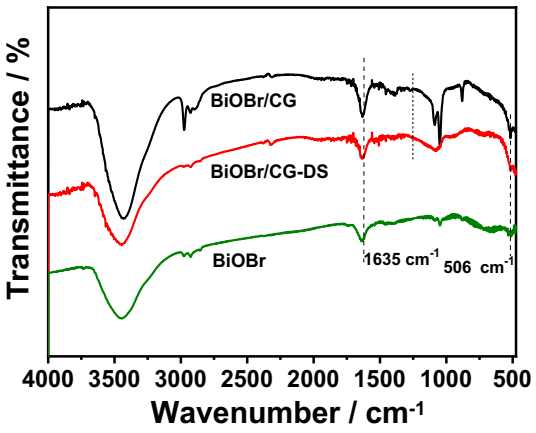

Fig. 5. FT-IR spectra of BiOBr, BiOBr/CG, and BiOBr/CG-DS.

in Figs. 1 and 2. The SEM images of BiOBr/CG and BiOBr/CG-DS have revealed that both possess similar micrometer microsphere structure incorporated with scattered individual thin graphitic-like sheets and narrow nanotubes, which are confirmed by the subsequent TEM characterization, as can be seen in Fig. 1a, b and Fig. 1c, d. For contrast with pure BiOBr in Fig. 1e, f, this 3D-like modular construction of BiOBr/C in Fig. 1g, h, BiOBr/CG and BiOBr/CG-DS is unchanged. Many radially grown nanosheets comprise an individual microsphere, in which these nanosheets interweave together as nanopores separate the nanosheets resulting in the open porous structure. TEM characterization has further evaluated the interior contact interface information from the interior architecture of the nanocomposite. The typical TEM images of BiOBr/CG-DS are shown in Fig. 2a-c. As seen in the figure, the lattice fringes are easily found, and the lattice spacing is approximately 2.82 Å between adjacent lattice planes, which is consistent with the *d*-spacing of the [012] reflection (2.82 Å) of BiOBr [28]. Moreover, several layers of the as-prepared graphitic-like sheets display wrinkled and transparent edges. TEM investigation has further confirmed that the electronic coupling between the BiOBr and the conductive network of graphitic-like sheets as well as carbon nanotubes should take place between the BiOBr [012] plane and the graphitic-like sheets and nanotubes [002] plane [29,30]. The presence of the large and closely contacted interface between the BiOBr and graphitic-like sheets as well as carbon nanotubes provides a favorable scenario for charge transfer between the three components.

3.2. Compositional and structural information

In order to explore the crystal phase and structure of the pure BiOBr and its composites, we have investigated the XRD patterns. Fig. 3 illustrates that all of the as-prepared samples display similar diffraction peaks in the XRD patterns, indicating that they were highly pure and crystalline devoid of impurity peaks for all samples. The XRD patterns are indexed to the tetragonal crystal phase of BiOBr (JCPDS file card no. 73-2061) [7]. Although, there is no apparent carbon structure diffraction (002) peak around 26.0° for CNT or graphene. This is most likely attributed to the overlapping of the main peak of the graphene-like materials around 26.0° and the (011) peak of tetragonal BiOBr at 25.3°, which strongly agrees with earlier reports of BiOBr/graphene [31]. It should be noted that incorporation of conjugated carbon does not change

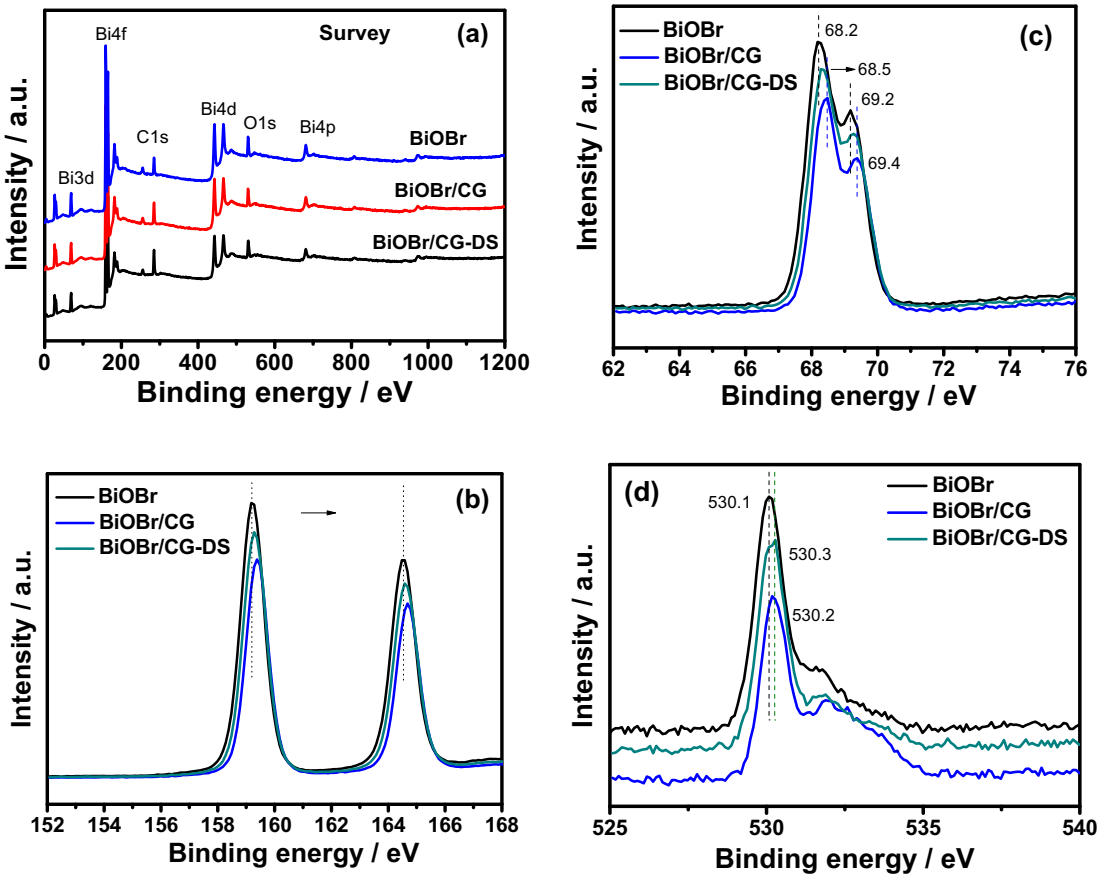

Fig. 6. XPS spectra of the BiOBr, BiOBr/CG, and BiOBr/CG-DS samples. (a) survey spectra, (b) Bi 4f core level, (c) Br 3d core level, (d) O 1s core level.

the crystal structure of BiOBr, however, the diffraction peaks of all nanocomposites slightly shifts to a lower angle compared to that of pure BiOBr. This shift suggests that the partial introduction of C atoms into BiOBr possibly induced crystal lattice defects, and lattice constant variation in BiOBr/CG-DS indicates the presence of certain interaction between the BiOBr crystal and graphitic-like structure after the solvothermal and sequent annealing reactions [5,32]. Furthermore, the relative intensity of the (001)/(110) peak of BiOBr/CG-DS greatly increases to 0.85 and that of BiOBr/CG increases to 0.75 from 0.25 for pure BiOBr, while the (001) peak of the BiOBr/CG-DS composite becomes relatively sharper after the occurred calcination process. This result can possibly be attributed to preferential attachment along the (001) plane and related structural combinations incorporated with graphitic-like structure and subsequent calcination [31].

We have further measured the Raman spectra of the synthesized samples in order to identify the existence of carbon structures in the different samples, as shown in Fig. 4. The composites clearly contain both the characteristic G bands (~1575.7 cm^{-1}, stretching of sp^2 carbon atom) and D bands (~1349.4 cm^{-1}, vibration of defect states), which are not observed in the pure BiOBr, further confirming the introduction of carbon structures [33]. This finding reveals that the BiOBr/C, BiOBr/CG, and BiOBr/CG-DS nanocomposites have been successfully constructed. After the calcining process, the typical G band for BiOBr/CG located at 1575 cm^{-1} has exhibited an obvious shift compared to that for BiOBr/CG-DS at 1601 cm^{-1}. This result indicates that the annealing treatment induced an interaction between the BiOBr and the conjugated graphitic-like structure. Generally, the intensity ratio of the D band and the G band (I_D/I_G) is calculated at 0.873 for BiOBr/CG, while after the calcining process, this value decreases to 0.825 for BiOBr/CG-DS. This observed decrease in the D/G intensity ratio indicates that the extent of defects/disorder in the oxygen-bearing graphitic-like structure decreases, leading to an increase in the average size of the sp^2 domains [26]. Next, we go on to confirm the chemical structure combination for BiOBr and BiOBr/CG, as well as its calcination composite, using FT-IR spectra, which are shown in Fig. 5. These FT-IR spectra shows low frequency peaks (at about 514 cm^{-1}) that are attributed to the asymmetrical stretching vibration of the Bi—O chemical bonds assigned to BiOBr, which are found in the spectra of BiOBr, BiOBr/CG, and BiOBr/CG-DS [12]. The characteristic absorption peak located at 1630 cm^{-1} that we observed in the FT-IR spectrum of the solvothermal product, BiOBr/CG, as well as its calcination product, BiOBr/CG-DS, could be assigned to the stretching vibrations of aromatic C=C [34]. Additionally, a characteristic peak around 1265 cm^{-1} is observed in BiOBr/CG nanocomposite that is absent in pure BiOBr, which could be mainly due to a probable Bi—C vibration [31,34]. The FT-IR analysis results show that the interaction between BiOBr and the conjugated carbon structure should be recognized due to the probable formation of Bi—C chemical bonding. Together with the XRD analysis, the FT-IR and Raman signals clearly indicate the successful synthesis of BiOBr/C, BiOBr/CG, and BiOBr/CG-DS nanocomposites.

Furthermore, in order to elucidate the surface element composition and the chemical state of elements in the BiOBr hybridized composite, we have carried out XPS spectra, displayed in Fig. 6. The resulting data from the survey of XPS spectra reveals that BiOBr and BiOBr/CG and its calcination product are composed of Bi, O, Br, and C elements (Fig. 6a). The high-resolution XPS spectra of Bi 4f (Fig. 6b) and Bi 3d (Fig. 6c) accurately displays two peaks.

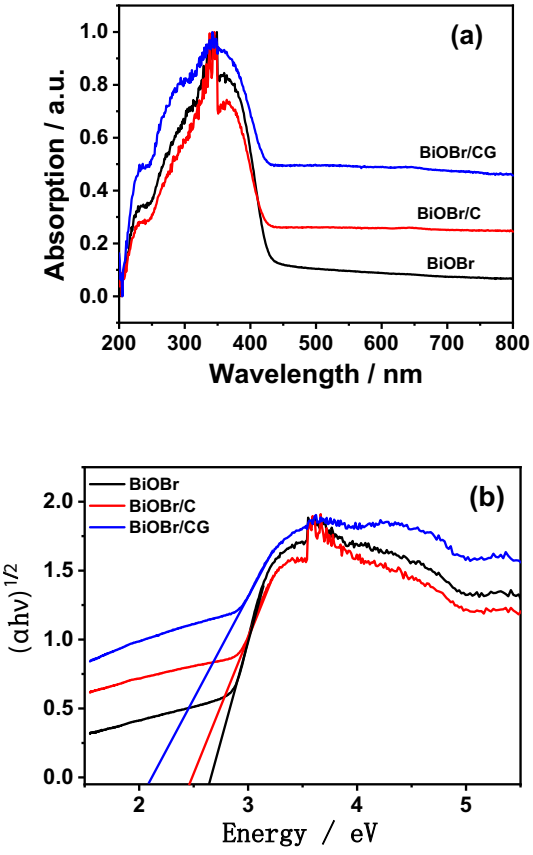

Fig. 7. DRS spectra (a) and the band gaps (*Eg*) of the different samples (b).

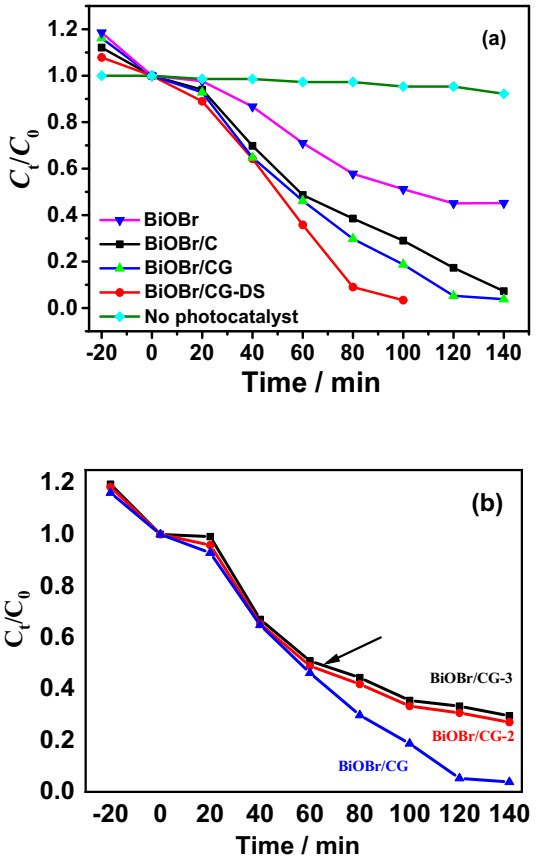

Fig. 8. Photocatalytic degradation of RhB with the different samples under visible light irradiation. (a: BiOBr, BiOBr/C, BiOBr/CG, BiOBr/CG-DS; b: series of BiOBr/CG samples with different amount of GO content).

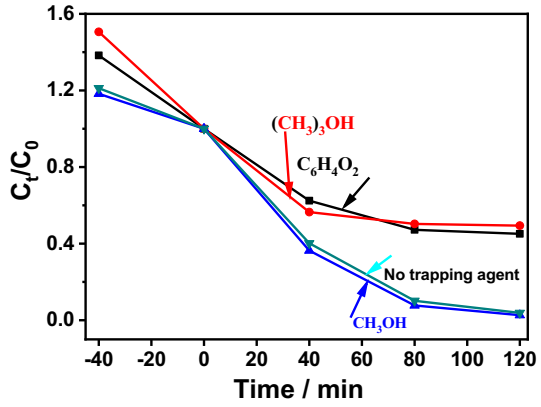

Fig. 9. Photodegradation dynamics of RhB in the presence of the BiOBr/CG-DS with and without addition of methanol, p-benzoquinone, and *t*-butyl alcohol.

Whereas, for pure BiOBr, there are two peaks of Bi $4f_{5/2}$ and Bi $4f_{7/2}$ at binding energies (BE) around 164.5 and 159.2 eV, while the Br $3d_{3/2}$ and $3d_{5/2}$ at BE of 69.2 and 68.2 eV, which are related to the Bi^{3+} and Br^{-} in BiOBr, respectively [5,6]. However, the peak BE of Bi 4f and Br 3d for BiOBr/CG and BiOBr/CG-DS are approximately 0.1–0.2 eV higher than that of bare BiOBr. This slight shift in the binding energy of Bi 4f and Br 3d in the BiOBr/CG and BiOBr/CG-DS hybrid indicates a variation in the electronic interaction between them, mainly resulting from some unpaired π electrons of the conjugated carbon atoms that could strongly interact with the free electrons on the surface of the BiOBr during the solvothermal or annealing treatment for the charge transfer transitions [31]. A similar phenomenon occurs in the O 1s spectrum of BiOBr, BiOBr/CG, and BiOBr/CG-DS, in which a wide and asymmetric peak is observed, and can be seen in Fig. 6d. When BiOBr coupled with conjugated graphitic-like structures, there is a slight shift of the peak position to a higher energy, when compared with pure BiOBr, to about 0.1 eV for BiOBr/CG and about 0.2 eV for BiOBr/CG-DS. This finding implies the formation of chemical bonds at the interface between the conjugated graphitic-like structures and the BiOBr (C—Bi or C—O—Bi bond) [35,36]. The observed shift in the peak positions in the Bi 4f and O 1s spectra provides information from which we can conclude that the formation of the Bi—C bond between the conjugated carbon and BiOBr as has been predicted by the XRD results.

3.3. Optical and photocatalytic properties

The ability of the synthesized samples for light absorption greatly affects their photocatalytic performance and further determines the generation of photogenerated electrons and holes [36]. Fig. 7 displays the UV–vis diffuse reflectance spectra of the BiOBr microspheres and its hybrids. Fig. 7a depicts the excellent visible light response of the BiOBr microspheres, which implies the possibility of photocatalytic activity under visible light irradiation. When compared to that of pure BiOBr, the light absorption of the BiOBr/CG sample shows a red shift and becomes strong in the visible region when combining with conjugated carbon structures. Contrastingly, BiOBr/C and BiOBr/CG both display excellent visible light absorption compared to pure BiOBr. The optical band gaps of BiOBr and its composites can be determined using the formula $(\alpha h\nu)^{1/2} = A(h\nu - Eg)$ by extrapolating the straight portion of $(\alpha h\nu)^{1/2}$ against the hν plot for an indirect bandgap transition, where α, h, ν, and A are the absorption coefficient, the Planck constant, the light frequency, and a constant, respectively [28,35]. According to the formula shown in Fig. 7b, the bandgap of pure BiOBr is calculated as 2.65 eV, whereas the bandgaps of BiOBr/C

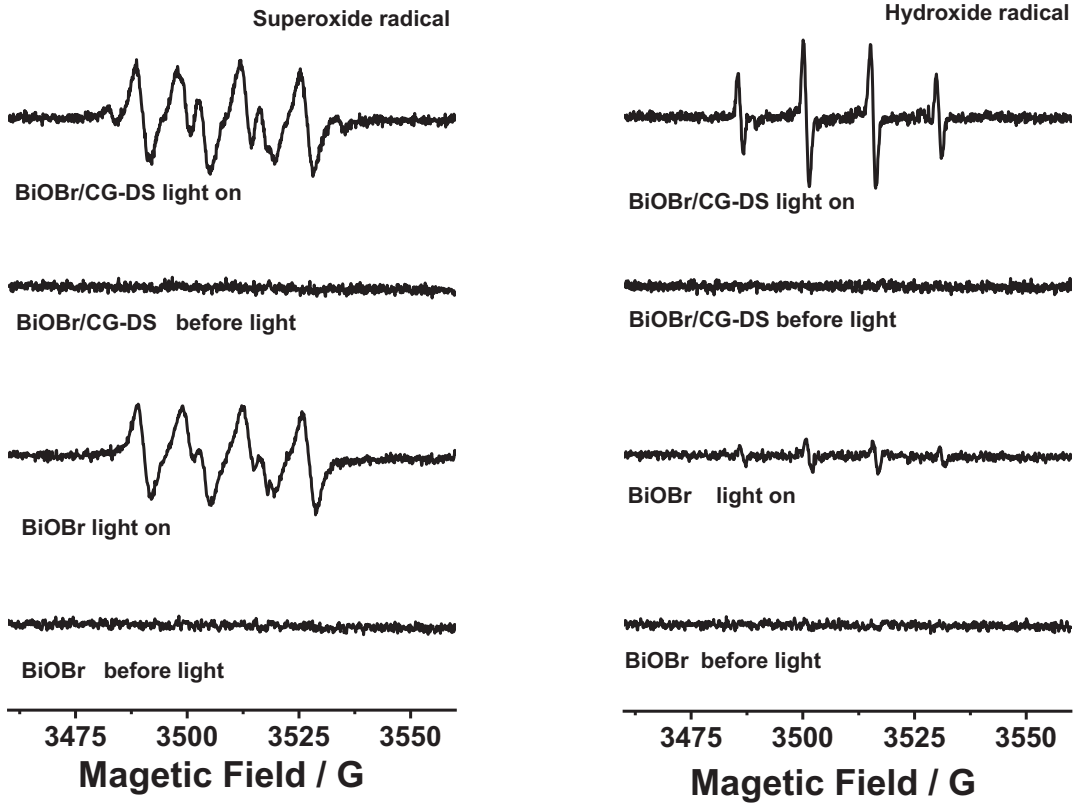

Fig. 10. ESR spectra of radical adducts trapped by DMPO (.O^{2-} and .OH) in the dark and under visible light irradiation.

and BiOBr/CG are variously reduced to 2.46 and 2.08 eV. This reason is that the solvothermal treatment for the charge transfer transitions improves the interfacial interaction between some of the conjugated carbon atom's unpaired π electrons and the free electrons on the surface of the BiOBr through the formation of probable chemical bonds between the BiOBr and the conjugated carbon structures, thus resulting in an upwards shift of the valence band edge and a reduction of the bandgap [31,33,37]. Therefore, the enhancement of the visible-light-responsive photocatalytic activity of the BiOBr photocatalyst can be directly ascribed to the introduction of highly efficient graphitic-like conductive network to BiOBr/CG, which causes the change in the bandgap.

We have evaluated and compared the photocatalytic activity of BiOBr and its series of hybrids to each other by examining the photodegradation of Rhodamine B (RhB) as a model pollutant under visible-light irradiation ($\lambda \geq 420$ nm) from a 500 W Xe lamp. To demonstrate the synergy-induced photocatalytic efficiency of the BiOBr/CG nanocomposite, we have performed contrastive experiments using pure BiOBr, BiOBr/C, BiOBr/CG-1, and BiOBr/CG-DS as photocatalysts for the photodegradation of RhB. Fig. 8 displays the time-dependent UV–vis absorption spectra of the aqueous solution of RhB (initial concentration, 10 mg/L) with the addition of 10 mg of the obtained BiOBr and its series of hybrids for various durations. The data shows that, in the blank experiment RhB is hardly degraded under visible light irradiation without the photocatalyst, indicating that the photocatalysis can be ignored (Fig. 8a). By comparison, the rate of RhB degradation in the presence of pure BiOBr is almost 55% after 120 min of irradiation. The results from the hybrids are more significant, and the photocatalytic activity of BiOBr/C increases intensively, reaching 83% degradation within 120 min, meanwhile the BiOBr/CG nanocomposite is exhibited very prominent photocatalytic efficiency, where 97% of the aqueous RhB solution is photodegraded under visible-light irradiation within the 120 min. Interestingly, the photocatalytic efficiency of the BiOBr/CG-DS nanocomposite could be further improved by annealing the BiOBr/CG product in atmospheric air. As shown in Fig. 8a, 97.9% of RhB is photodegraded in the presence of the annealed BiOBr/CG-DS after only 100 min of visible-light irradiation. It is reasonable that the high temperature (400 °C) would normally induce a greater number of defects onto the graphitic-like surface, which would result in greater adsorption or photocatalytic sites for organic dyes. Through further testing, we have presented data to support the influence of varying amounts of GF on the photocatalytic degradation of RhB, which are presented in Fig. 8b. It can be seen that, within in 120 min, both BiOBr/CG-2 and BiOBr/CG-3 can accomplish a maximum level of RhB degradation of almost 70%, whereas, BiOBr/C without GF can remove 83% of the RhB during that time. BiOBr/CG, BiOBr/CG-2, and BiOBr/CG-3 have distinct photocatalytic degradation efficiencies, a finding which illustrates a key role for the construction of effective conductive pathways through the dispersive CNT/GF network in high efficiency electron-hole separation and transfer. Furthermore, the improvement in photocatalytic efficiency in BiOBr/CG and its annealing product, BiOBr/CG-DS, indicates that introducing a graphitic-like structure into the composite, as well as its further annealing, enhance the photocatalytic activity remarkably. We believe this may be attributed to the interactions between the conjugated carbon structures and BiOBr , as previously shown by TEM and XRD.

3.4. Opto-electronic properties

In order to explore the catalytic role of various active free radicals generated in the reaction system, we have conducted a trapping experiment of active species, which is shown in Fig. 9. We have used methanol, p-benzoquinone, and *t*-butyl alcohol (TBA) as the trapping quenchers for h+, $\cdot O^{2-}$, and ·OH, respectively [38,39]. As shown in Fig. 9, when methanol is added as a scavenger for h^+, the efficiency of RhB photo-degradation is only slightly depressed, indicating that the h^+ plays a negligible role during the photocatalytic reaction. However, when p-benzoquinone and *t*-butyl alcohol (TBA) are added as scavengers for $\cdot O^{2-}$or ·OH, the efficiency of RhB photo-degradation decreased sharply, indicating that the $\cdot O^{2-}$ and ·OH are main active species during the photocatalytic reaction. This result identifies that, in the photocatalytic system, the $\cdot O^{2-}$ and ·OH are responsible for the enhanced photocatalytic activity.

To further confirm the primary active species generated for pure BiOBr and BiOBr/CG-DS during the photocatalytic reaction, we have performed the ESR spin-trap with DMPO techniques under visible light irradiation. We find no signals in the dark for pure BiOBr and BiOBr/CG-DS; however, we could clearly observe the characteristic peaks of DMPO-$\cdot O^{2-}$ and DMPO-·OH for pure BiOBr and BiOBr/CG-DS under light irradiation, as shown in Fig. 10. It is important to note that the signal intensity of trapped -·OH is obviously stronger for the BiOBr/CG-DS composite than for pure BiOBr. This result suggests that signals for both $\cdot O^{2-}$ and -·OH in present system occur under visible light irradiation and that the corresponding amount of -·OH radicals in the reaction sys-

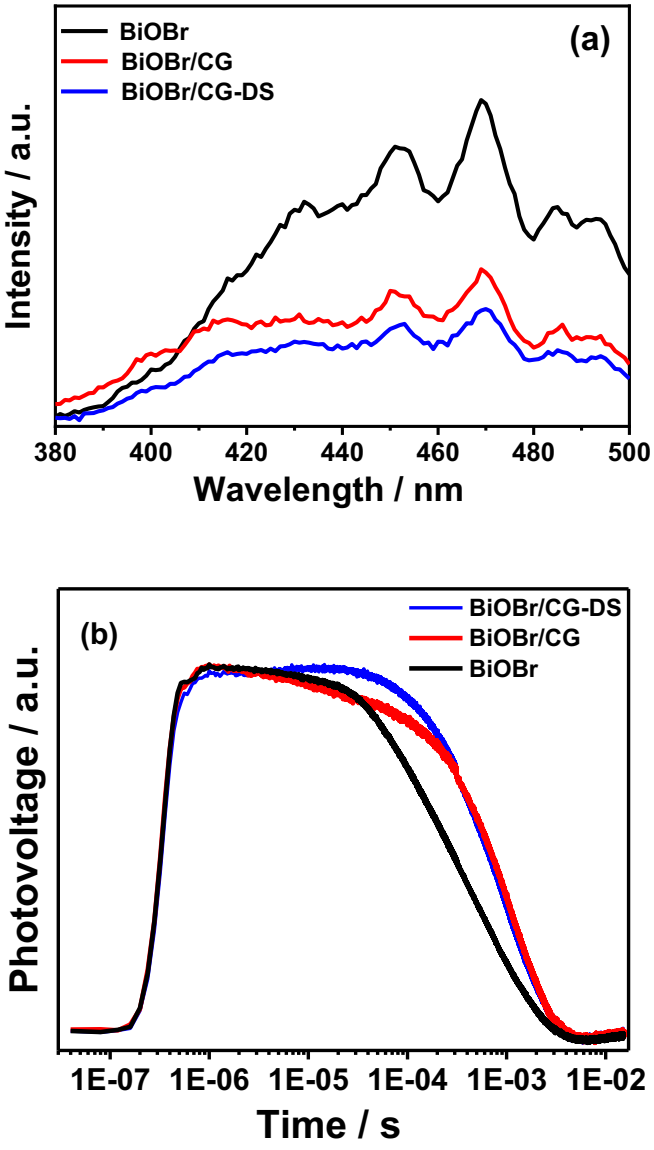

Fig. 11. PL (a) and SPV (b) of pure BiOBr, BiOBr/CG, and BiOBr/CG-DS samples.

tem with the BiOBr/CG-DS composite looks greater than that of BiOBr alone. The ESR results suggest that $\cdot O^{2-}$ and -·OH are the main active species in the photocatalytic reaction, which are well consistent with the results from the trapping experiment for the active species in the presence of different scavengers.

The photocatalytic performance of semiconductor photocatalysts largely depends on the recombination efficiency of pairs (REPEH), and the REPEH is indirectly influenced by the PL intensity and the photoelectrocurrent density (PEC) [28]. We have first investigated the photogenerated electron/hole separation and their lifetime by PL spectroscopy (Fig. 11a). After excitation at 300 nm, pure BiOBr has exhibited a broad PL, ranging from 380 to 550 nm. After association with graphitic-like structures, the PL signal shapes for BiOBr/CG and its annealing product are not altered, but their intensity decreases markedly, indicating that recombination of their electron/hole pair in BiOBr has been inhibited after combination. Moreover, SPV technique also provides credible information on photocatalytic samples with respect to charge transfer and separation in space [24]. For pure BiOBr, BiOBr/CG, and its annealing product, the SPV response signals display intensities of similar strength (Fig. 11b). Despite this, the downward trend in the SPV response signal becomes slower in the time scale for BiOBr/CG and its annealing product, whereas, the signal for BiOBr/CG-DS decreases most slowly, indicating that BiOBr/CG-DS has the longest charge separation time, which are consistent with the results of the PL intensity experiment.

To further substantiate the efficient separation of photogenerated electron/hole pairs, we have compared the photocurrent responses through the irradiation of BiOBr and BiOBr/CG-DS films on an ITO substrate under Xe lamp irradiation [11]. As shown in Fig. 12, the photocurrent response stays stable and reversible during the repeated switching on and off cycles, suggesting efficient charge separation and collection. Under light irradiation, the measured photocurrent for BiOBr deposited on ITO is approximately 0.71×10^{-6} A/cm^{-2}. After association with RGO and CNT, the photocurrent density increases to approximately 1.57×10^{-6} A/cm^{-2}, this is contrary to the BiOBr film electrode results and almost two times higher than that of BiOBr/CG-DS. The photocurrent densities of the BiOBr/CG-DS composites are in good accordance with their photocatalytic activities, indicating that the separation and transfer of the photogenerated charges to the working electrodes in the BiOBr/CG-DS composite is more efficient as well as faster.

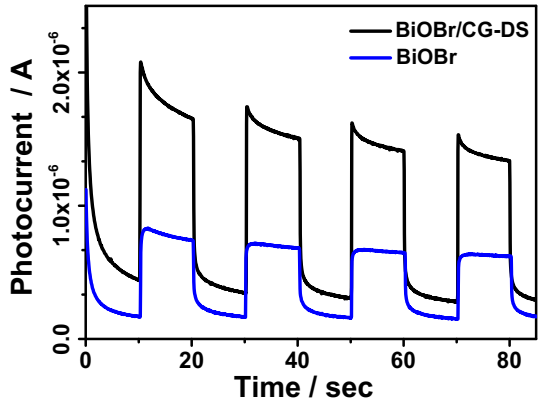

Fig. 12. Transient photocurrent responses of pure BiOBr and BiOBr/CG-DS samples.

On the basis of the previously described experimental data, we can explain the photocatalytic mechanism of BiOBr/CG-DS, which is summarized and illustrated in Fig. 13: Under visible light irradiation, BiOBr crystals can be excited to introduce electrons to the CB, leaving holes in the VB. The photogenerated electrons in the CB of BiOBr could easily transfer to effective conductive networks due to the electron storing and shuttling ability of the graphene-like carbon structures and the internal electron field at the BiOBr/CG interface [39]. The photogenerated electron/hole recombination in BiOBr is also greatly inhibited by the increased VB width and the upshifting of CB [40], as previously demonstrated by PL and PEC measurements. Meanwhile, the electrons collected on the surface of the graphene-like conductive networks can react with oxygen molecules adsorbed at the surface of the photocatalyst to produce $O_2\cdot^-$ radicals. The holes in the VB of BiOBr directly react with H_2O molecules to give ·OH radicals, and finally, the RhB dye is greatly photodegraded by the photo generated $O_2\cdot^-$ and ·OH radicals. Thus, in BiOBr/CG-DS, effective graphene-like conductive networks and intimate interfacial interaction can effectively accelerate the charge transfer and suppress charge recombination, ultimately leaving more charge carriers and thereby promoting the degradation of dyes.

4. Conclusion

We have fabricated a self-assembled nanocomposite of 3D BiOBr hybridized with 1D CNT and 2D RGO in situ with a method that employed a facile solvothermal (BiOBr/CG) and subsequent annealing (BiOBr/CG-DS) process, forming a 3D globular structure about 5 μm in diameter with about 20 nm lamellar layers chemically bonded with CNT and RGO. We have observed superior photocatalytic activity for RhB degradation under visible light irradiation with the BiOBr/CG composite compared to the BiOBr and BiOBr/C composites. Further annealing treatment of the as mentioned samples results in remarkable improvement in photocatalytic performance. Based on the characterization carried out

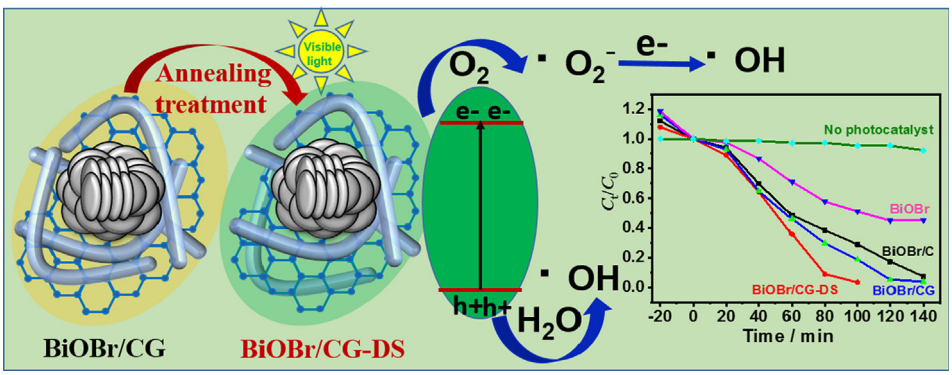

Fig. 13. Graphical representation of catalytic mechanism in microscopic nanostructure of BiOBr/CG and BiOBr/CG-DS.

herein, the enhanced photocatalytic activity of the BiOBr/CG-DS nanocomposite is mainly attributed to the effective interface interaction between BiOBr and the conductive network of graphitic-like flakes with CNTs, which acts as a productive electron transfer bridge that yields a more efficient charge transfer and charge separation. An indirect dye photosensitization process is the dominant driver of the photodegradation in the BiOBr/CG-DS system, with photogenerated $O_2^{\cdot -}$ and ·OH radicals as the main reactive species. These results reveal the effective design of a highly efficient, cost-effective, and environmentally benign photocatalyst with visible light activity, and shed light on its potential for commercial use in environmental remediation and energy conversion.

Declaration of Competing Interest

The authors declare that they have no known competing financial interests or personal relationships that could have appeared to influence the work reported in this paper.

Acknowledgments

This research was supported by the National Natural Science Foundation of China (61605167 and 11804289), China; the Program for Innovative Research Team (in Science and Technology) at the University of Henan Province (19IRTSTHN026), China; the Outstanding Young Backbone Teacher Funding Project of Xuchang University, China; Zhongyuan Scholars (202101510004) and Zhongyuan Thousand Talents Project of Henan Province (204200510016), China. SH Lee would like to thank to the support of the National Research Foundation of Korea (NRF) grant funded the Korea government (MSIT) (No. 2019R1A5A8080326).

References

[1] P. Zhou, J. Yu, M. Jaroniec, All-solid-state Z-scheme photocatalytic systems, Adv. Mater. 26 (2014) 4920–4935.
[2] Y. Li, P. Zhang, D. Wan, C. Xue, J. Zhao, G. Shao, Direct evidence of 2D/1D heterojunction enhancement on photocatalytic activity through assembling MoS2 nanosheets onto super-long TiO2 nanofibers, Appl. Surf. Sci. 504 (2020) 144361.
[3] C.B. Ong, L.Y. Ng, A.W. Mohammad, A review of ZnO nanoparticles as solar photocatalysts: synthesis, mechanisms and applications, Renew. Sustain. Energy Rev. 81 (2018) 536–551.
[4] Z. Wang, Z. Chu, C. Dong, Z. Wang, S. Yao, H. Gao, Z. Liu, Y. Liu, B. Yang, H. Zhang, Ultrathin BiOX (X = Cl, Br, I) nanosheets with exposed 001 facets for photocatalysis, ACS Appl. Nano Mater. 3 (2020) 1981–1991.
[5] L. Allagui, B. Chouchene, T. Gries, G. Medjahdi, E. Girot, X. Framboisier, A.B.h. Amara, L. Balan, R. Schneider, Core/shell rGO/BiOBr particles with visible photocatalytic activity towards water pollutants, Appl. Surf. Sci. 490 (2019) 580–591.
[6] C. Liu, X. Dong, Y. Hao, X. Wang, H. Ma, X. Zhang, Efficient photocatalytic dye degradation over Er-doped BiOBr hollow microspheres wrapped with graphene nanosheets: enhanced solar energy harvesting and charge separation, RSC Adv. 7 (2017) 22415–22423.
[7] F.S. Jun Zhang, Jing Lin, Dongfeng Chen, Jianming Gao, Zhixin Huang, Xiaoxia Ding, Chengcun Tang, Self-assembled 3-D architectures of BiOBr as a visible light-driven photocatalyst, Chem. Mater. 20 (2008) 2937–2941.
[8] X. Xiong, L. Ding, Q. Wang, Y. Li, Q. Jiang, J. Hu, Synthesis and photocatalytic activity of BiOBr nanosheets with tunable exposed 0 1 0 facets, Appl. Catal. B 188 (2016) 283–291.
[9] Y. Mi, H. Li, Y. Zhang, N. Du, W. Hou, Synthesis and photocatalytic activity of BiOBr nanosheets with tunable crystal facets and sizes, Catal. Sci. Technol. 8 (2018) 2588–2597.
[10] H. Li, J. Liu, T. Hu, N. Du, S. Song, W. Hou, Synthesis of belt-like BiOBr hierarchical nanostructure with high photocatalytic performance, Mater. Res. Bull. 77 (2016) 171–177.
[11] W. Tie, J. Jin, S.S. Bhattacharyya, H. Yue, Y. Lei, Z. Zheng, W. He, S.H. Lee, Covalent bonding of ZnO nanostructures with dispersible carbon nanotubes for self-assembly photocatalytic heterostructures, Appl. Surf. Sci. 492 (2019) 219–227.
[12] C. Zhao, W. Li, Y. Liang, Y. Tian, Q. Zhang, Synthesis of BiOBr/carbon quantum dots microspheres with enhanced photoactivity and photostability under visible light irradiation, Appl. Catal. A 527 (2016) 127–136.
[13] F. Chen, Q. Yang, S. Wang, F. Yao, J. Sun, Y. Wang, C. Zhang, X. Li, C. Niu, D. Wang, G. Zeng, Graphene oxide and carbon nitride nanosheets co-modified silver chromate nanoparticles with enhanced visible-light photoactivity and anti-photocorrosion properties towards multiple refractory pollutants degradation, Appl. Catal. B 209 (2017) 493–505.
[14] D. Liu, J. Xie, Y. Xia, Improved photocatalytic activity of MWCNT/BiOBr composite synthesized via interfacial covalent bonding linkage, Chem. Phys. Lett. 729 (2019) 42–48.
[15] K. Liu, P. Zhang, F. Miao, S. Zhang, Y. Zhang, G. Cao, G. Shao, High-quality rGO/MoS2 composite via a facile "prereduction-microwave" strategy for enhanced lithium and sodium storage, J. Alloys Compd. 821 (2020).
[16] S. Shoji, H. Suzuki, R.P. Zaccaria, Z. Sekkat, S. Kawata, Optical polarizer made of uniaxially aligned short single-wall carbon nanotubes embedded in a polymer film, Phys. Rev. B 77 (2008).
[17] W. Shim, Y. Kwon, S.Y. Jeon, W.R. Yu, Optimally conductive networks in randomly dispersed CNT:graphene hybrids, Sci. Rep. 5 (2015) 16568.
[18] A.A. Maarouf, A. Kasry, B. Chandra, G.J. Martyna, A graphene–carbon nanotube hybrid material for photovoltaic applications, Carbon 102 (2016) 74–80.
[19] G. Cao, Z. Liu, P. Feng, Y. Zhao, J. Niu, Concave ultrathin BiOBr nanosheets with the exposed 001 facets: room temperature synthesis and the photocatalytic activity, Mater. Chem. Phys. 199 (2017) 131–137.
[20] W. Tie, S.S. Bhattacharyya, Y. Zhang, Z. Zheng, T.H. Lee, S.W. Lee, T.H. Kim, Y.H. Lee, S.H. Lee, Field-induced stretching and dynamic reorientation of functionalized multiwalled carbon nanotube aggregates in nematic liquid crystals, Carbon 96 (2016) 548–556.
[21] W. Tie, S.S. Bhattacharyya, Y. Wang, W. He, S.H. Lee, Facile in-situ synthesis of a zinc oxide crystals/few-layered graphene flake composite for enhanced photocatalytic performance, J. Photochem. Photobiol., A 348 (2017) 89–95.
[22] P. Bindu, S. Thomas, Estimation of lattice strain in ZnO nanoparticles: X-ray peak profile analysis, J. Theoret. Appl. Phys. 8 (2014) 123–134.
[23] K.S. Subrahmanyam, S.R.C. Vivekchand, A. Govindaraj, C.N.R. Rao, A study of graphenes prepared by different methods: characterization, properties and solubilization, J. Mater. Chem. 18 (2008) 1517–1523.
[24] Y. Lei, L. Gu, W. He, Z. Jia, X. Yang, H. Jia, Z. Zheng, Intrinsic charge carrier dynamics and device stability of perovskite/ZnO mesostructured solar cells in moisture, J. Mater. Chem. A 4 (2016) 5474–5481.
[25] X. Zhang, Y. Feng, S. Tang, F. Wei, Preparation of a graphene oxide–phthalocyanine hybrid through strong π–π interactions, Carbon 48 (2010) 211–216.
[26] Y. Chen, F. Sun, Z. Huang, H. Chen, Z. Zhuang, Z. Pan, J. Long, F. Gu, Photochemical fabrication of SnO 2 dense layers on reduced graphene oxide sheets for application in photocatalytic degradation of p -Nitrophenol, Appl. Catal. B 215 (2017) 8–17.
[27] Z. Cui, K. Gao, S. Ge, W. Fa, Solvothermal modification of BiOCl nanosheets with Bi nanoparticles using ascorbic acid as reductant and the superoxide radicals dominated photocatalytic performance, Mater. Res. Express 4 (2017).
[28] J. Chen, X. Xiao, Y. Wang, M. Lu, X. Zeng, Novel AgI/BiOBr/reduced graphene oxide Z-scheme photocatalytic system for efficient degradation of tetracycline, J. Alloys Compd. 800 (2019) 88–98.
[29] L. Li, R. Bao, J. Yi, L. Liu, S. Mao, Preparation of CNT/Cu nano composite powder with uniform dispersion and strong interface bonding by SP method, Powder Technol. 325 (2018) 107–112.
[30] Z. Chen, R. Wu, Y. Liu, Y. Ha, Y. Guo, D. Sun, M. Liu, F. Fang, Ultrafine Co nanoparticles encapsulated in carbon-nanotubes-grafted graphene sheets as advanced electrocatalysts for the hydrogen evolution reaction, Adv. Mater. 30 (2018) e1802011.
[31] X. Tu, S. Luo, G. Chen, J. Li, One-pot synthesis, characterization, and enhanced photocatalytic activity of a BiOBr-graphene composite, Chemistry 18 (2012) 14359–14366.
[32] Y. Sun, K. Xu, Z. Wei, H. Li, T. Zhang, X. Li, W. Cai, J. Ma, H.J. Fan, Y. Li, Strong electronic interaction in dual-cation-incorporated NiSe2 nanosheets with lattice distortion for highly efficient overall water splitting, Adv. Mater. 30 (2018) e1802121.
[33] H. Moussa, E. Girot, K. Mozet, H. Alem, G. Medjahdi, R. Schneider, ZnO rods/reduced graphene oxide composites prepared via a solvothermal reaction for efficient sunlight-driven photocatalysis, Appl. Catal. B 185 (2016) 11–21.
[34] S. Vadivel, P. Keerthi, M. Vanitha, A. Muthukrishnaraj, N. Balasubramanian, Solvothermal synthesis of Sm-doped BiOBr/RGO composite as an efficient photocatalytic material for methyl orange degradation, Mater. Lett. 128 (2014) 287–290.
[35] N. Song, H. Fan, H. Tian, Reduced graphene oxide/ZnO nanohybrids: metallic Zn powder induced one-step synthesis for enhanced photocurrent and photocatalytic response, Appl. Surf. Sci. 353 (2015) 580–587.
[36] H. Li, T. Hu, N. Du, R. Zhang, J. Liu, W. Hou, Wavelength-dependent differences in photocatalytic performance between BiOBr nanosheets with dominant exposed (0 0 1) and (0 1 0) facets, Appl. Catal. B 187 (2016) 342–349.
[37] B. Li, T. Liu, Y. Wang, Z. Wang, ZnO/graphene-oxide nanocomposite with remarkably enhanced visible-light-driven photocatalytic performance, J. Colloid Interface Sci. 377 (2012) 114–121.
[38] Y. Chen, F. Sun, Z. Huang, H. Chen, Z. Zhuang, Z. Pan, J. Long, F. Gu, Photochemical fabrication of SnO 2 dense layers on reduced graphene oxide sheets for application in photocatalytic degradation of p -nitrophenol, Appl. Catal. B Environ. (2017). S0926337317304526.
[39] R.T. Thomas, P. Abdul Rasheed, N. Sandhyarani, Synthesis of nanotitania decorated few-layer graphene for enhanced visible light driven photocatalysis, J. Colloid Interface Sci. 428 (2014) 214–221.
[40] J. Chen, M. Guan, W. Cai, J. Guo, C. Xiao, G. Zhang, The dominant 001 facet-dependent enhanced visible-light photoactivity of ultrathin BiOBr nanosheets, PCCP 16 (2014) 20909–20914.